8-2024

THE ROLE OF EFFLUX PUMP INHIBITOR IN ENHANCING ANTIMICROBIAL EFFICIENCY OF SILVER NANOPARTICLES AND METHYLENE BLUE AS AN EFFECTIVE PHOTODYNAMIC THERAPY AGENT

Yaran Allamyradov

THE ROLE OF EFFLUX PUMP INHIBITOR IN ENHANCING ANTIMICROBIAL EFFICIENCY OF SILVER NANOPARTICLES AND METHYLENE BLUE AS AN EFFECTIVE PHOTODYNAMIC THERAPY AGENT

A Thesis submitted in partial fulfillment
of the requirements for the degree
Master of Science

Department of Physics and Astronomy
Western Kentucky University
Bowling Green, Kentucky

By
Yaran Allamyradov

August, 2024

The Role of Efflux Pump Inhibitor in Enhancing Antimicrobial Efficiency of Silver Nanoparticles and Methylene Blue as an Effective Photodynamic Therapy Agent

Yaran Allamyradov

Date Recommended 7/8/2024

DocuSigned by:
ali oguz er
F0511F8EF47B4C8...
Chair

DocuSigned by:
Ivan Novikov
D1F15C9383BB48E...
Committee Member

DocuSigned by:
Simran Banga
6922DD3BDFD14B9...
Committee Member

Committee Member

DocuSigned by:
Jennifer Hammonds
EBE3858E068F42D...
Executive Director for Graduate Studies

ABSTRACT

THE ROLE OF EFFLUX PUMP INHIBITOR IN ENHANCING ANTIMICROBIAL EFFICIENCY OF SILVER NANOPARTICLES AND METHYLENE BLUE AS AN EFFECTIVE PHOTODYNAMIC THERAPY AGENT

Efflux pumps are critical active transport systems utilized by cells to expel toxic substances, including antibiotics and photosensitizer complexes, thereby contributing to antimicrobial resistance. Efflux pump inhibitors (EPIs), which are compounds that obstruct the transport of molecules through these pumps, play a pivotal role in enhancing the effectiveness of antimicrobial therapies against pathogens. This study investigates the effects of the EPI reserpine on the photodeactivation rate of pathogens when used in conjunction with silver nanoparticles (Ag NPs) and methylene blue (MB), a common photosensitizer.

Our research reveals that the application of reserpine, in combination with Ag NPs and MB, leads to a significantly higher rate of pathogen deactivation compared to the use of Ag NPs and MB alone. This enhanced deactivation rate suggests that reserpine plays a crucial role in disrupting the cellular mechanisms that typically expel these toxic agents. To understand the underlying mechanisms, we examined the generation of singlet oxygen, a reactive oxygen species known to play a role in photodeactivation.

Additionally, we tested different sizes of Ag NPs in combination with reserpine to determine if nanoparticle size influences the effectiveness of this treatment. The results indicate that reserpine consistently improves the deactivation rate, regardless of the size of the Ag NPs. Molecular docking calculations were performed to investigate the affinity of reserpine and MB for the AcrB protein, a component of the AcrAB-TolC efflux pump. These calculations demonstrated that reserpine has a higher affinity for AcrB compared to MB.

The significant improvement in bacterial deactivation observed in our study is primarily attributed to the blockage of the AcrAB-TolC efflux pump by reserpine. This blockage prevents the removal of MB from the cells, thereby enhancing the photodeactivation process. The increased deactivation rate is not due to enhanced singlet oxygen production, but rather the effective retention of MB within the cells.

I dedicate this thesis to my family and fiancée for their endless support throughout my academic career.

ACKNOWLEDGEMENTS

Firstly, I extend my deepest gratitude to Dr. Ali Oguz Er for his support and trust throughout these two years. His patience, even during the most unproductive phases of my research, has been invaluable. I liken his mentorship to the careful preparation of my bacterial cultures. He provided the ideal environment for my growth, ensuring optimal conditions—down to the precise temperature—and patiently waited for my development until I produced valuable results. Unlike my bacteria that were deactivated after incubation, he nurtured me into starting my PhD journey.

I am also immensely grateful to Dr. John Andersland for his training on TEM and SEM, and for his challenging questions that deepened my understanding and simplified problem-solving in my research. My thanks also go to Dr. Banga for her insightful advice on the microbial world.

A special thanks to Justice ben Yosef for teaching me experimental techniques and consistently supporting me in data collection. I appreciate Salizhan Kylychbekov for demonstrating the heights of hard work and determination. Additionally, I thank Inomjon Majidov and Zikrulloh Khuzhakulov for their unwavering support.

Lastly, I thank all the bachelor's and Gatton Academy students who endured my poor jokes and patiently participated in my sometimes tedious PDT experiments.

CONTENTS

LIST OF FIGURES

CHAPTER 1

INTRODUCTION

1.1 Antibiotic resistance

Antibiotic resistance is a significant and rapidly growing problem that is exacerbated by the excessive use of antibiotics and insufficient infection control measures. This issue is widely recognized as one of the most pressing public health challenges of our time due to its widespread impact and the alarming rate at which it occurs. According to a recently published report by the Center for Disease Control and Prevention (CDC), it is estimated that nearly three million antibiotic-resistant infections occur in the United States each year, resulting in the deaths of over 35,000 individuals[1]. The transmission of antibiotic-resistant bacteria and fungi is not confined to one region but can spread globally through the movement of people, animals, and goods. Antibiotic resistance is a grave threat to homeland security, as highlighted in the report "Antibiotic Resistance Threats in the United States" by the Homeland Security Digital Library[2]. It compromises our ability to treat infections effectively, potentially leading to severe public health crises and jeopardizing national safety. Given the rising prevalence of pathogens resistant to both antibiotics and antiseptics, there is an urgent need for alternative antimicrobial strategies that can effectively inactivate pathogens without promoting resistance. Some of the promising alternatives to traditional antibiotics include the use of predatory bacteria, antimicrobial peptides, bacteriophages, gene editing enzymes, metals, and photodynamic therapy (PDT)[3].

1.2 Photodynamic therapy

Among the various methods proposed to combat this issue, PDT stands out as a particularly promising area of research, driven by the continuous discovery of new synthetic and natural photosensitizers (PS). An ideal PS should have a high absorption wavelength to ensure

deeper tissue penetration and effective singlet oxygen production, while also being cost-effective[4–6]. PDT operates by generating reactive oxygen species, such as hydroxyl radicals and singlet oxygen, through the application of light, which can then be used to target and treat bacteria, cancerous cells, and other diseased cells[5,7,8]. The ability of PDT to eliminate antibiotic-resistant germs has made it a viable alternative to traditional antibiotics. PDT has demonstrated efficacy in treating bacterial infections, particularly in the fields of dermatology and oncology[9–13]. For instance, phenothiazine dyes are applied to the affected skin areas and subsequently activated by red light, leading to the destruction of the targeted pathogens.

1.3 PLAL synthesis of Ag NPs and their role in PDT

Nanomaterials, particularly those with dimensions less than 100 nm, have captivated scientific interest due to their distinctive properties, which differ significantly from bulk materials. This unique behavior is largely attributed to surface effects, a high surface-to-volume ratio, and quantum confinement effects[14,15]. Ag NPs are among the most studied due to their remarkable optical, magnetic, electronic, and chemical properties. Various synthesis methods exist, but Pulsed Laser Ablation in Liquid (PLAL) has emerged as a prominent technique due to its simplicity, rapidity, and eco-friendliness[16].

PLAL involves focusing a high-intensity laser pulse on a metal target submerged in a liquid medium. This process generates a plasma plume at the target surface, leading to the formation of nanoparticles. The nanoparticles are then dispersed in the liquid, resulting in a colloidal solution. The size and characteristics of the produced nanoparticles can be controlled by adjusting laser parameters such as wavelength, energy, fluence, repetition rate, and ablation time, as well as modifying the properties of the ablation solvent[14].

The type and concentration of the liquid medium significantly affect nanoparticle synthesis. For instance, Mafuné *et al*. demonstrated that increasing the concentration of sodium dodecyl sulfate (SDS) in an aqueous solution led to smaller Ag NP sizes[17]. Similarly, polyvinylpyrrolidone (PVP) as a stabilizing agent increased nanoparticle formation efficiency while reducing their size. The ablation efficiency and nanoparticle stability also vary with different solvents, such as deionized water, ethanol, and acetone.

The pulse width of the laser impacts nanoparticle size and shape. Longer ablation times generally result in smaller nanoparticles due to increased fragmentation and reduced aggregation. Studies have shown that ablation times ranging from 5 to 120 minutes can produce nanoparticles with mean diameters as small as 2 nm[18,19].

The unique properties of Ag NPs make them suitable for a wide range of applications. Their strong surface plasmon resonance (SPR) enables their use in optical and biosensing applications[20]. Ag NPs also exhibit excellent thermal and electrical conductivity, making them ideal for electronic circuits, inks, and adhesives[21]. Their antibacterial, antiviral, and antifungal properties are harnessed in medical applications, including wound dressings, coatings for medical devices, and drug delivery systems. Additionally, Ag NPs are used in catalysis, water treatment, and food preservation due to their chemical stability and catalytic activity[21–23].

Ag NPs have demonstrated significant potential in enhancing the efficacy of PDT. PDT relies on photosensitizing agents to produce reactive oxygen species (ROS) when exposed to specific wavelengths of light, leading to the destruction of targeted cells, such as cancer cells or bacteria. The combination of Ag NPs with traditional photosensitizers like methylene blue (MB) has shown to improve the antimicrobial and anticancer properties of PDT[24].

Our group, previously synthesized Ag NPs using pulsed laser ablation in various aqueous solutions, including polyvinylpyrrolidone (PVP), citrate, and deionized water, and characterized them using techniques like transmission electron microscopy (TEM) and UV-Vis spectroscopy[24]. When combined with MB, these Ag NPs significantly enhanced the generation of singlet oxygen, a crucial ROS in PDT, compared to MB alone. This synergistic effect was attributed to the ability of Ag NPs to increase the photostability and singlet oxygen yield of MB, making the PDT process more effective[24,25].

1.4 Efflux pumps and their inhibitors

One of the primary mechanisms through which bacteria develop antibiotic resistance is through the action of membrane protein complexes known as efflux pumps. These efflux pumps are active transporters that enable bacterial cells to expel toxic substances, including antibiotics and photosensitizer complexes, from within the cell. EPIs are compounds designed to obstruct the passage of molecules through these efflux pumps, thereby enhancing the efficacy of antimicrobial agents. Reserpine, a medication commonly used to manage blood pressure in combination with a thiazide diuretic or a vasodilator, is one example of an EPI. By inhibiting the function of efflux pumps, EPIs can play a crucial role in mitigating antibiotic resistance and improving the effectiveness of treatments like PDT[26,27].

Reserpine functions as a sympatholytic and antihypertensive medication through multiple mechanisms, primarily by inhibiting the absorption of adrenergic neurotransmitters and binding

to catecholamine storage vesicles, which include neurotransmitters such as dopamine and norepinephrine. Specifically, reserpine irreversibly inhibits VMAT-2 (vesicular monoamine transporter-2), a crucial component in the adrenergic neurotransmission pathway. By blocking VMAT-2, reserpine effectively prevents the transportation of serotonin, norepinephrine, and dopamine into presynaptic storage vesicles. This inhibition results in a depletion of these neurotransmitters from the presynaptic neurons, thereby reducing their availability for release into the synaptic cleft. Consequently, the reduced levels of these neurotransmitters lead to a decrease in sympathetic nervous system activity, which in turn helps to lower blood pressure and exert its antihypertensive effects.

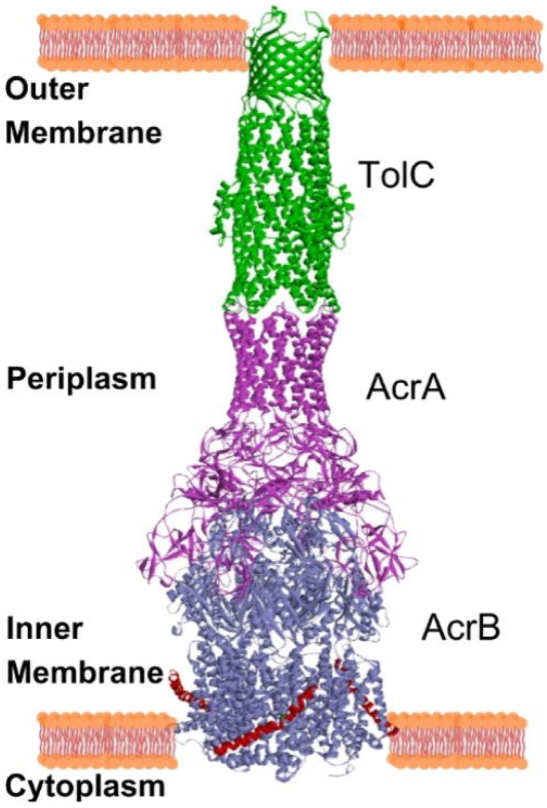

Figure 1.Schematic representation of the AcrAB-TolC multidrug efflux pump of the Gram-negative bacteria E. Coli generated using BIOVIA Discovery Studio.

Escherichia coli (*E. coli*) is equipped with numerous efflux pumps that play a vital role in expelling metabolic waste, toxic substances, and antimicrobial agents from the cellular matrix[28,29]. Among these efflux pumps, one prominent example is the AcrAB-TolC efflux pump, which is a homotrimer, tripartite system composed of three key proteins: the inner membrane protein acriflavine resistance protein B (AcrB), the outer membrane protein TolC, and the membrane fusion protein acriflavine resistance protein A (AcrA), as depicted in Figure 1.

The AcrAB-TolC efflux pump is highly versatile, capable of *extruding* a wide range of substances including multiple antibiotics, dyes, bile salts, and detergents[30]. The activity of the AcrB protein, which belongs to the resistance-nodulation-division (RND) family, is intricately coupled to the proton gradient across the bacterial membrane. This coupling mechanism allows the efflux pump to utilize the energy stored in the proton gradient to drive the extrusion of various compounds from both the bacterial cytoplasm and the periplasm into the extracellular matrix[31].

It has been demonstrated that these efflux pumps are not only essential for the bacteria's ability to remove harmful substances but also play a critical role in antibiotic resistance m[32,33]. By actively transporting antimicrobial agents out of the bacterial cell, the AcrAB-TolC efflux pump significantly reduces the intracellular concentration of these agents, thereby diminishing their efficacy and contributing to the bacteria's survival in the presence of antibiotics. This multifaceted functionality of the AcrAB-TolC efflux pump underscores its importance in the overall physiology and pathogenicity of *E. coli*, highlighting the need for strategies to inhibit these pumps as part of efforts to combat antibiotic resistance.

The synergistic application of nanoparticles in combination with antibiotics has been proposed as an innovative strategy to treat infections caused by multidrug-resistant (MDR) and extensively drug-resistant (XDR) bacteria[34,35]. One key mechanism by which nanoparticles exhibit antimicrobial activity is through the inhibition of efflux pumps. This can occur either by directly binding to the active sites of these pumps or by disrupting their efflux kinetics[36]. When nanoparticles are used in conjunction with antibiotics, the required concentration of both agents can be reduced, thereby diminishing the overall drug dosage and the associated toxicity to human cell lines[37].

Studies have shown that phenothiazinium dyes such as toluidine blue O (TBO), methylene blue (MB), and dimethylmethylene blue (DMMB) are substrates of major facilitator superfamily (MFS) pumps, such as NorA in *Staphylococcus aureus*. These dyes are also substrates for resistance-nodulation-division (RND) efflux pumps in *Escherichia coli* (AcrAB-TolC) and *Pseudomonas aeruginosa* (MexAB-OprM)[38,39]. Efflux pumps not only render antimicrobial agents ineffective by removing them from within the cell but also decrease the intracellular concentration of these agents, thus contributing significantly to antibiotic resistance. *Therefore, targeting efflux pump complexes is crucial for overcoming antibiotic-resistant bacteria.*

Studies have demonstrated that the use of reserpine can enhance the efficacy of PDT[40]. Recent studies have shown that PDT utilizing MB and TBO exhibited enhanced photocytoplasmic toxicity against *Pseudomonas aeruginosa* and *Staphylococcus aureus* in the presence of EPIs compared to photosensitizers alone[38,39]. Additionally, MB-EPI complexes have been synthesized as substrates for efflux pumps to maximize the antibacterial effects against methicillin-resistant *Staphylococcus aureus* (MRSA), *Escherichia coli*, and *Acinetobacter baumannii*[41,42]. It was also observed that the timing of EPI addition, either before or after the photosensitizer, has different impacts. Introducing the EPI increased the PDT effect of phenothiazine dyes but not nonphenothiazine dyes[41]. Various mechanisms have been proposed for the action of EPIs, including increasing cell permeability to photosensitizers, reducing the cells' antioxidant defenses, and disrupting membrane potential, leading to a loss of the proton motive force[38,41,42].

Despite these advances, the direct effect of the EPI reserpine in conjunction with MB and nanoparticles has not been thoroughly investigated. In this study, we explored whether reserpine

could enhance the antibacterial effect in the photodeactivation of pathogens when used with Ag NPs and MB[43]. Ag NPs were synthesized in citrate solutions using nanosecond laser pulses. These Ag NPs were then combined with MB to increase singlet oxygen generation and photo-responsivity. Our findings demonstrated that the combination of MB, Ag NPs, and reserpine was a more effective antibacterial agent compared to the combination of MB and Ag NPs alone. This suggests that reserpine, when used in conjunction with Ag NPs and MB, can significantly improve the efficacy of antibacterial PDT, offering a promising approach to combat antibiotic-resistant bacterial infections.

CHAPTER 2

MATERIALS AND METHODS

2.1 Synthesis of Ag NPs

Ag NPs were synthesized in a solution containing sodium citrate, which acts as a stabilizer to prevent particle aggregation. Sodium citrate was purchased from Fisher Scientific. The synthesis of Ag NPs involved irradiating a silver plate using a Nd:YAG laser beam (Continuum Surelite II) with a repetition rate of 10 Hz and a pulse duration of 5 ns, at wavelengths of 1064 nm and 532 nm.

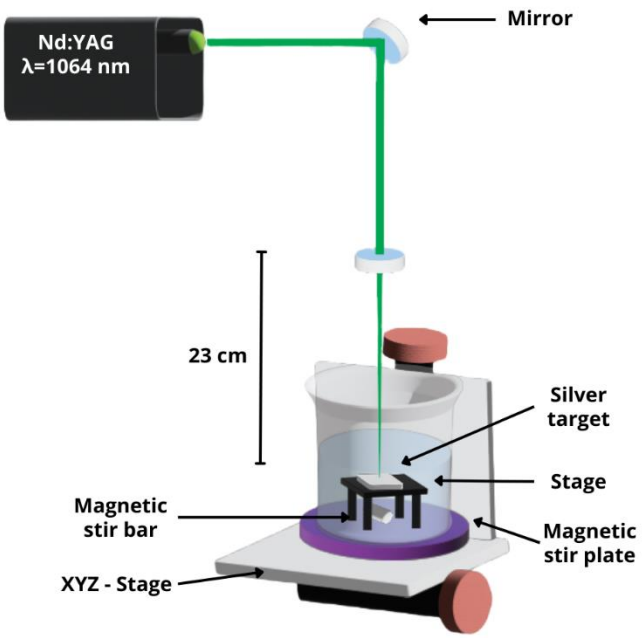

Figure 2 Experimental setup for the pulsed laser ablation in liquid for AuNP synthesis.

The silver target used was 99.99% pure, with dimensions of 1.0 mm thickness and 1 × 1 inch width and length, secured on a small aluminum table using double-sided carbon tape. The setup included placing the aluminum table with the silver target and a magnetic stirring bar inside a 50 ml beaker, followed by adding 24 ml of a specified aqueous solution to achieve a solution height of 11 mm above the target.

Throughout the synthesis process, the 50 ml beaker was placed on a magnetic stir plate to ensure continuous stirring, preventing the accumulation of Ag NPs above the target and minimizing shielding effects. An XY-translational stage was positioned under the magnetic stir plate, continuously moving in XY directions to achieve uniform ablation of the target, as depicted in Figure 2.

For the 1064 nm wavelength, the laser operated at 200 mJ per pulse. A converging lens with a focal length of 30 cm was used to focus the laser beam onto the target, positioned 23 cm above the target to achieve a laser beam spot size of 1 mm after focusing. Each synthesis session lasted 10 minutes.

2.2 Characterization of Ag NPs

The Ag NP solutions were characterized using transmission electron microscopy (TEM). For TEM sample preparation, a drop-cast technique was employed: 3 μL of the Ag NP solution was deposited onto a 300-Mesh Copper TEM grid and allowed to air-dry.

After obtaining TEM images, ImageJ software was utilized for automated size measurement of the produced Ag NPs and to generate size distribution data. This process involved applying Gaussian Blur to the images, reducing image contrast to minimize background interference, setting a threshold to encompass the maximum number of nanoparticles, and measuring the Feret diameter (the longest particle dimension). These measurements, totaling 150 nanoparticles (n = 150), were used to construct size distribution histograms and calculate the average Feret diameter and standard deviation.

In addition to TEM characterization, the synthesized Ag NPs were analyzed using UV-Visible Spectroscopy, Fluorescence Spectroscopy, and Fourier Transform Infrared (FTIR) Spectroscopy.

2.3 Reactive Oxygen Species Generation Measurement

To confirm and measure the production of reactive oxygen species (ROS) induced by MB in combination with Ag NPs, a colorimetric assay was conducted using 9,10-Anthracenediyl-bis(methylene)dimalonic Acid (ABMDMA). ABMDMA has an absorption peak at 400 nm. In the presence of ROS, ABMDMA undergoes a reaction where oxygen adds in a 2+4 cycloaddition, forming an endoperoxide. This reaction reduces the aromatic π-electron system, causing the optical properties to fade. Therefore, the absorbance of the solution directly indicates the level of ROS generated.

Experimental solutions were prepared by combining the desired reagents, which included MB (6.0×10^{-5} M), Ag NPs, and reserpine, with 100 μL of a 2.4 mM ABMDMA solution in a 1.5 mL cuvette. The total volume was adjusted to 1 mL using phosphate buffer solution (PBS). Initial absorbance measurements were taken for each cuvette before irradiation. Subsequently, each cuvette was exposed to irradiation for the specified duration. After irradiation, absorbance measurements were taken again to confirm the production of reactive oxygen species (ROS).

2.4 Bacteria deactivation

To assess the efficacy of Ag NPs combined with MB for PDT in vitro, Gram-negative bacteria *E. coli* were subjected to irradiation in the presence and absence of these compounds. *E. coli* was initially inoculated in LB Broth and incubated for 18-24 hours at 37°C with constant mixing at 200 rpm. Following incubation, the culture was diluted to achieve an absorbance of approximately 1.7 at 600 nm, corresponding to a bacterial concentration of approximately 10^8 colony-forming units per milliliter (CFU/mL).

Bacterial samples containing experimental solutions were prepared in individual wells of a six-well plate, following the experimental setup depicted in Figure 3. The concentrations of

each compound tested were carefully controlled: MB at 0.03 µM, commercially produced Ag NPs at 0.025 mg/mL, experimentally produced Ag NPs at 0.0095 mg/mL, and Reserpine at 8 µM.

To ensure uniform mixing and distribution of the compounds, the plate was covered with aluminum foil to prevent unintended exposure to light. It was then placed on a shaker plate and agitated at 100 rpm for 10 minutes. This step ensured thorough mixing of the bacterial suspension with the compounds.

After mixing, the aluminum foil was removed, and the plate was subjected to irradiation using a 660 nm red LED lamp (Bestqool, 105 W) for a specified duration. The lamp was positioned 9 cm above the plate to maintain consistent light fluence across all wells, as depicted in Figure 3.

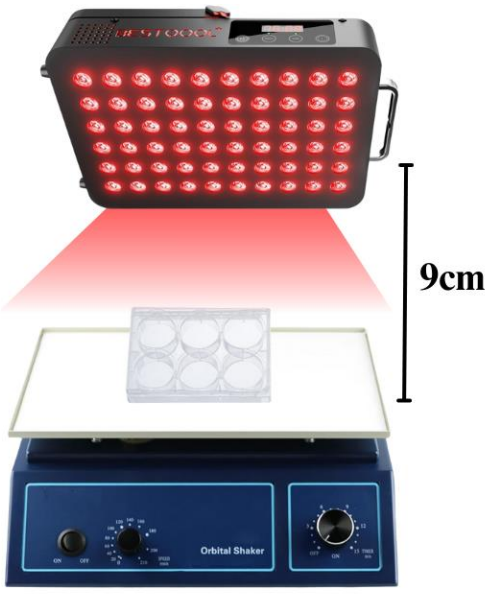

Figure 3 Photodynamic therapy bacteria deactivation experimental setup

Following irradiation, each bacterial solution underwent serial dilution to reduce bacterial density. The diluted solutions were then plated onto agar plates and incubated at 37°C for 18-24 hours. During this incubation period, viable bacterial colonies formed on the agar plates.

After completion of the incubation period, the plates were examined, and the number of bacterial colonies on each plate was counted. This counting process allowed for the assessment of bacterial viability and provided quantitative data on the effectiveness of the experimental compounds and light treatment in reducing bacterial growth.

2.5 Molecular docking

Molecular docking using Autodock Vina was conducted following previously established methods[44,45]. The exhaustivity parameter was set to 16 for enhanced precision in the docking calculations. Ligand structures, including Reserpine (PubChem CID 5770) and Methylene blue (PubChem CID 6099), were obtained in SDF format from the PubChem library. These files were converted to PDB format using Open Babel for compatibility with Autodock Tools. Subsequently, the ligands were prepared in Autodock Tools by allowing all rotatable bonds to optimize their conformations.

The protein structure used for docking was sourced from the PDB file 2DRD, obtained from RCSB PDB. In preparation, two subunits of a homotrimer and the embedded ligand (minocycline) were removed to isolate the target binding pocket. Charges and hydrogen atoms were added to the protein structure to ensure accurate simulation conditions.

A search box with dimensions of 30 $Å^3$ was centered within the identified drug-binding pocket of the protein. This configuration facilitated precise docking simulations to predict the binding affinities and orientations of Reserpine and MB within the protein's active site.

2.6 TEM images

Cells were initially treated with light to initiate the experimental conditions. For primary fixation, the cells were transferred into 1.5 mL microfuge tubes, and 80 µL of 25% glutaraldehyde was added to each tube. The tubes were capped, inverted, and left to sit for 10

minutes at room temperature. Following this, the cells were centrifuged at 5,000 rpm for 5 minutes, and the supernatant was carefully removed and discarded as glut waste. To wash the cells, 1 mL of PBS was added to resuspend the pellet, and the mixture was centrifuged again at 5,000 rpm for 5 minutes at room temperature. The supernatant was discarded as glut waste. This washing step was repeated, leaving 50 µL of PBS in the tubes after the second wash.

For embedding in agarose, the pellet tubes were placed on ice while the agarose tubes were maintained in a 42°C water bath. Subsequently, 50 µL of 42°C 4% agarose was pipetted into each tube, mixed by pipetting, and the tubes were centrifuged at 5,000 rpm for 5 minutes in a preheated centrifuge at 40°C. The tubes were immediately placed on ice to solidify the agarose. Once the agarose hardened, it was carefully removed from the tubes using a spatula and cut into 1x1x0.5 mm slices on a plastic lid using a one-sided razor. These slices were then transferred to vials containing PBS.

To prepare for osmium tetroxide post-fixation, half of the samples were treated by adding 0.5 mL of cold 3% glucose to non-osmium tetroxide tubes and vials, while the other half received 0.5 mL of cold 3% glucose with 1% osmium tetroxide. It was crucial not to resuspend the pellets in the tubes during this step. The samples were incubated on ice for 30 minutes, and the solutions were carefully removed and disposed of as osmium waste.

For the washing steps, cold DI water was gently added to the tubes and vials without resuspending the pellets, and the mixture was left to sit on ice for 10 minutes. This wash step was repeated twice, with the water solutions being removed each time and discarded as osmium waste. The dehydration process involved sequential treatment with 0.5 mL of ethanol at concentrations of 25%, 50%, 75%, 95%, and three changes of 100%, ensuring the solutions

remained cold through the 75% ethanol step, with 25% and 50% ethanol wastes disposed of as osmium waste.

The cells were then infiltrated with Spurr's resin by treating them with 0.5 mL of 33%, 66%, 95%, and 100% resin for 30 minutes each at room temperature. Following a second treatment with 100% resin, the samples were left overnight in the refrigerator. The next morning, fresh 100% resin was added, and the agarose pieces were oriented into molds using microfuge tubes as molds for the pellets. Labels were inserted as required.

Finally, the samples were polymerized by placing the molds in an incubator at 70°C for 20 hours, after which they were promptly removed.

CHAPTER 3

RESULTS AND DISCUSSION

In this study, we examined the impact of reserpine on the photodeactivation of pathogens, focusing particularly on gram-negative bacteria *E. coli*. Our investigation centered on understanding how reserpine influences treatments involving MB alone and in combination with silver nanoparticles (Ag NPs/MB).

The hypothesis proposed that by inhibiting the efflux pump with reserpine, the intracellular concentrations of MB and Ag NPs could be elevated. This elevation was expected to enhance the phototoxic effects of PDT specifically targeted at bacterial cells, while concurrently minimizing potential risks to neighboring host cells from exposure to singlet oxygen.

3.1 Characterization of Ag NPs

The characterization experiment results revealed that the synthesized silver nanoparticles had an average size of 6.61 nm with a standard deviation of 3.21 nm, indicating a relatively uniform size distribution. The size distribution histogram showed that most of the nanoparticles

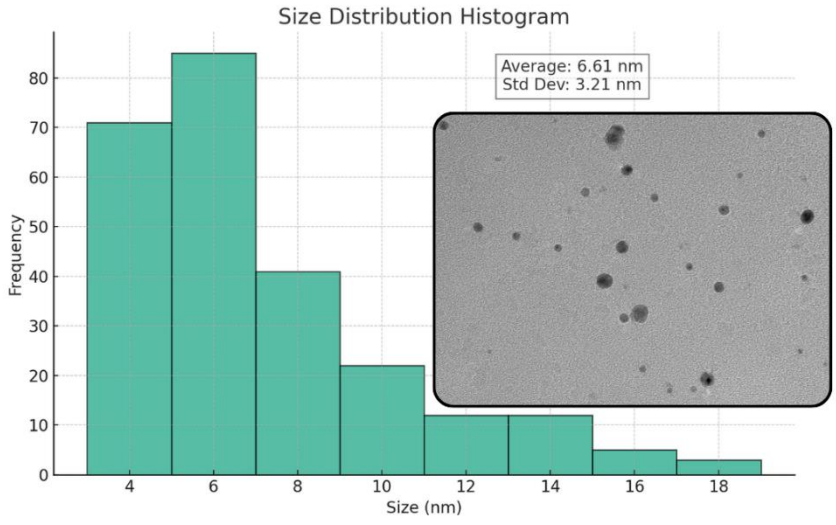

Figure 4 Size distribution of Ag NPs synthesized in 2 mM citrate.

were within the 4-8 nm range, with the highest frequency around 6 nm. There was a noticeable right skew in the distribution, with fewer nanoparticles exceeding 8 nm in size. Additionally, TEM imaging confirmed the nanoparticle sizes, supporting the histogram data and demonstrating the successful synthesis of silver nanoparticles with consistent size characteristics (Figure 4).

The characterization of silver nanoparticles synthesized in 2 mM citrate was conducted using FTIR and UV-Vis spectroscopy. The FTIR spectrum exhibited distinct absorption bands, notably the O-H stretching vibration around 3100-3600 cm^{-1} and the C=O stretching vibration between 1700-1750 cm^{-1}. These peaks suggest the presence of hydroxyl and carbonyl functional groups, indicative of successful stabilization of the nanoparticles by citrate molecules (Figure 5).

The UV-Vis absorbance spectrum of the silver nanoparticles showed a prominent peak at approximately 400 nm, characteristic of the surface plasmon resonance (SPR) of silver nanoparticles. This peak confirms the formation of silver nanoparticles and indicates their nanoscale dimensions (Figure 5).

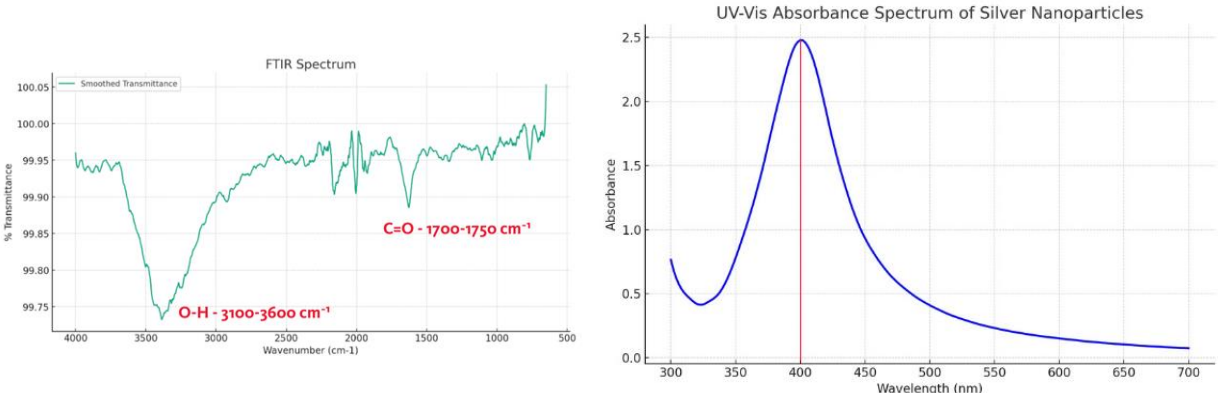

Figure 5 FTIR and UV-Vis Spectroscopy of Ag NPs synthesized in 2 mM citrate.

3.2 Bacteria deactivation measurement.

Figure 6 illustrates the deactivation rate of *E. coli* colonies over irradiation time on a logarithmic scale. When MB was used alone, approximately 10^5 colonies remained after 10 minutes of irradiation. However, when MB was combined with silver nanoparticles (Ag

NPs/MB), bacterial survival was reduced to zero after 8 minutes of irradiation. The effect of reserpine in conjunction with MB or MB/Ag NPs became increasingly pronounced over time, as evident from the logarithmic nature of the graph. Specifically, the difference in deactivation rates between MB alone and MB/reserpine was more substantial at 10 minutes compared to 8 minutes, and even more so at 8 minutes compared to 6 minutes of irradiation.

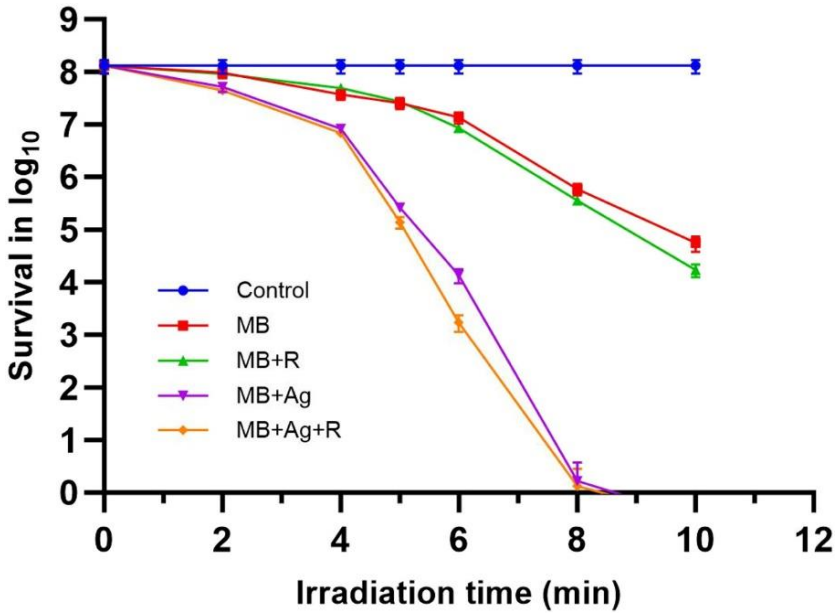

Figure 6 Colony formation unit with respect to time after treatment with MB, Ag NPs, and reserpine and irradiated with 664 nm light.

Ag NPs are well-known for their antimicrobial properties, attributed to mechanisms such as the release of Ag+ ions and increased surface area that damages bacterial cell walls[46–48]. In this study, we aimed to mitigate their antimicrobial effects by using a concentration significantly below the standard minimum inhibitory concentration (MIC) and a brief incubation period of 10 minutes before irradiation [49]. Our results indicate that neither reserpine nor Ag NPs alone exhibited a statistically significant reduction in bacterial populations under the given conditions (data not shown for clarity). However, when reserpine and Ag NPs were used in combination with MB, there was a substantial increase in photodeactivation efficacy. This enhancement was

observed to be time-dependent, with complete deactivation of bacteria achieved after 8 minutes of irradiation, prompting further investigation at 6 minutes of irradiation time (Figure 7).

Figure 7 demonstrates the photodeactivation rate after 6 minutes of irradiation. When reserpine was used with MB, there was an additional 40% reduction in colony-forming units (CFU) compared to MB alone. In contrast, a 90% reduction was observed when reserpine was used with Ag NPs/MB compared to Ag NPs/MB alone.

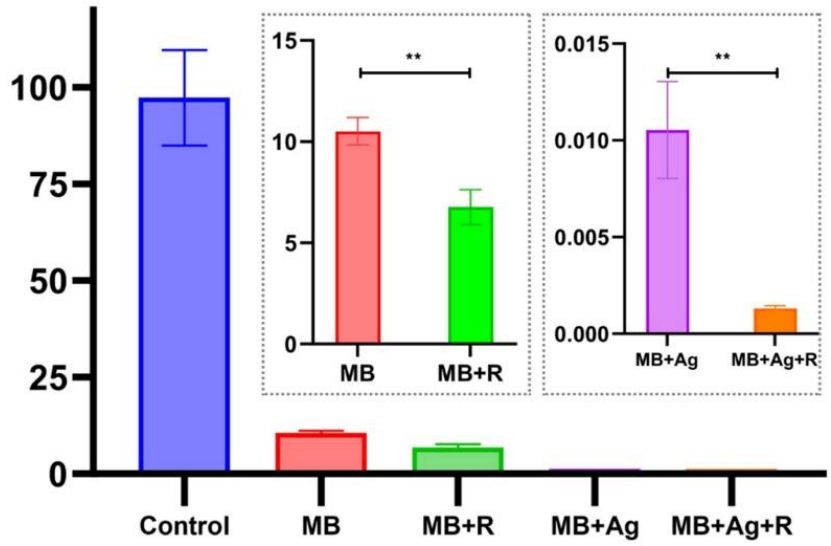

Figure 7 CFU count of E. Coli with MB, Ag NPs, and/or reserpine after 6 min of irradiation. Insets how lower concentrations in detail. Independent samples t-test revealed a statistically significant difference between MB and MB+R ($p < 0.01$) and between MB+Ag and MB+Ag+R ($p < 0.01$).

It has been proposed that metal nanoparticles might disrupt the proton motive force, which is an essential element for the operation of functional efflux pumps[50–52]. For instance, the inhibitory effect of zinc oxide nanoparticles on NorA efflux pumps in *S. aureus* has been previously examined[53]. The study showed a significant increase in inhibition zone areas for ciprofloxacin, with a 27% increase in *S. aureus* and a 22% increase in *E. coli* when ZnO nanoparticles were present. Additionally, copper nanoparticles have been found to alter the outer membrane permeability of P. aeruginosa, partially due to the generation of Cu(II) ions from the

copper nanoparticles[34]. These released Cu(II) ions may disrupt the membrane potential, ultimately affecting the functionality of efflux pumps.

A specific study demonstrated the loss of membrane potential in *E. coli* cells, showing a reduction from −185 mV to −104 mV and −77 mV after exposing the bacterial cells to 3.0 μg/ml and 7.5 μg/ml concentrations of copper nanoparticles, respectively, for one hour[54]. Furthermore, poly(acrylic)-acid coated iron oxide nanoparticles have been shown to inhibit drug efflux, leading to a higher intracellular drug concentration in Mycobacterium smegmatis [50,55].

Ag NPs are among the most extensively used due to their potent antimicrobial activity. The primary mechanism behind the antimicrobial effect of Ag NPs is believed to be the release of Ag+ ions and the increased surface area, which ultimately damages the bacterial cell wall. The impact of Ag NPs on the disruption of the efflux kinetics of the multidrug resistance (MDR) efflux pump, MexAM-OPrM, in *P. aeruginosa* has already been investigated[56]. In our study, the role of silver as an EPI could account for the further reduction observed when used in conjunction with MB, as illustrated in Figures 6 and 7.

3.3 Size of Ag NPs nanoparticles on reserpine

It has been demonstrated that smaller Ag NPs are more effective in PDT due to their higher surface area to volume ratio, which facilitates greater accumulation inside cells[24,57]. Building on this observation, we investigated the impact of different sizes of Ag NPs to assess whether reserpine exhibits size-dependent activity. Three commercially produced Ag NPs ranging from 10 nm to 40 nm were utilized to evaluate size effects, and specifically, to determine if reserpine's efficacy varied with nanoparticle size.

Our experiments reaffirmed the established correlation that smaller Ag NPs are more effective, as they generate higher concentrations of singlet oxygen, as depicted in Figure 8. This heightened singlet oxygen production translates to a more potent antibacterial effect[57].

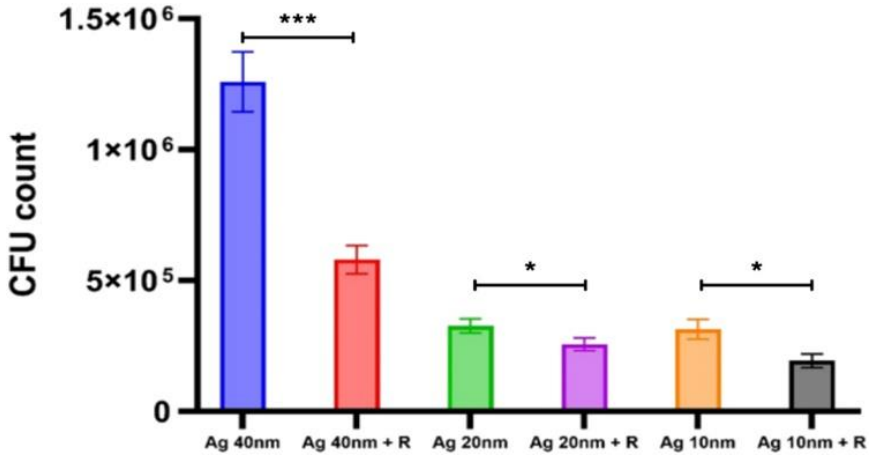

Figure 8 CFU count comparing the effect of treatment using various sizes of Ag NPs with and without reserpine after 5 min of irradiation. Independent samples t-test revealed a statistically significant difference between Ag 40 nm and Ag 40 nm + R ($p < 0.001$), between Ag 20 nm and Ag 20 nm + R ($p < 0.05$), and between Ag 10 nm and Ag 10 nm + R ($p < 0.05$).

However, our current findings did not reveal a discernible relationship between reserpine's effectiveness and the size of Ag NPs. Regardless of nanoparticle size (40 nm, 20 nm, or 10 nm), reserpine consistently enhanced the bactericidal efficacy of Ag NPs. The presence of reserpine resulted in reductions in surviving bacteria by 54.75%, 33.64%, and 43.81%, respectively, for the three nanoparticle sizes.

It is important to note that while no direct size-dependent relationship was observed for reserpine, its beneficial impact was consistently observed across all experiments involving Ag NPs. This underscores reserpine's potential as a potent adjunct in enhancing the antimicrobial activity of PDT, irrespective of nanoparticle size.

3.4 Bacterial uptake and morphology change measurements

To examine potential morphological changes during treatment, bacteria were preserved in resin following a 3-minute irradiation period. This duration was chosen to allow simultaneous observation of both deactivated and viable bacteria. Figure 9 illustrates: a) the control sample, b) the effects of irradiation with Ag NPs and MB, and c) the combination of MB, Ag NPs, and reserpine.

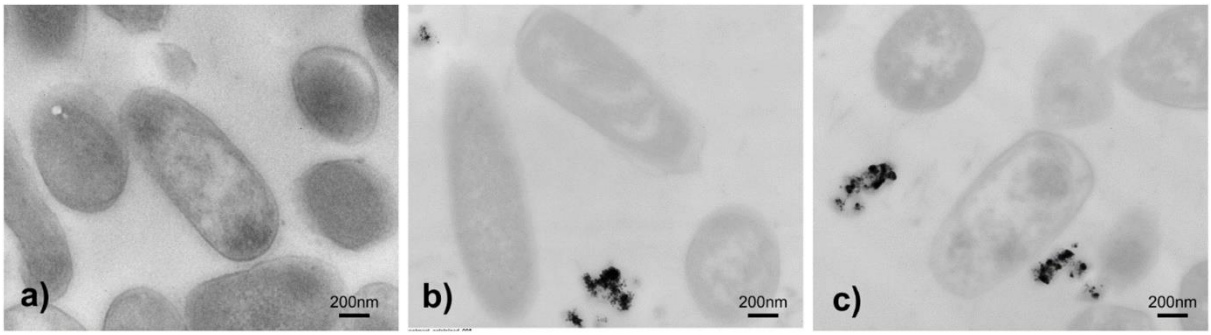

Figure 9. TEM images of bacteria after 3 min of irradiation with 660 nm LED light, a) control, b) MB with Ag NPs, c) MB, Ag NPs with reserpine.

Following irradiation and fixation, it was observed that Ag NPs tended to aggregate alongside debris from deactivated bacteria in samples with and without reserpine. Interestingly, samples treated with reserpine showed an expanded periplasmic space, which appeared wider compared to both non-reserpine-treated samples and the control.

The aggregation of nanoparticles with different charges is typically influenced by various factors such as solution temperature, pH, particle size, van der Waals forces, and electrostatic repulsion among particles[58]. The observed enlargement of the periplasmic space in reserpine-treated samples could potentially be attributed to the inhibition of efflux pumps. This morphological change may also result from interactions between MB, Ag NPs, and bacterial cell walls.

3.5 Singlet oxygen generation

To investigate the mechanism behind the observed increase in PDT efficacy and determine whether reserpine affects singlet oxygen generation, singlet oxygen production was measured by analyzing the photobleaching of the 400 nm absorption band of ABMDMA after varying irradiation times, as described in the materials and methods section.

Singlet oxygen generation efficiency is known to be proportional to the population of excited triplet photosensitizers produced via intersystem crossing (ISC) from excited singlet photosensitizers. The efficiency of singlet oxygen generation can be enhanced with the use of heavy atoms[59]. In nanoparticle systems, efficient intraparticle energy transfer contributes to enhanced singlet oxygen generation, as observed in photosensitizer-doped conjugated polymer nanoparticles[60].

Figure 10 depicts singlet oxygen generation in different solutions in the absence of bacteria. When reserpine was added to MB alone, there was no observable change in the 400 nm band, indicating that reserpine did not influence singlet oxygen production in solution. However, when reserpine was added to the MB/Ag NPs solution, a slight decrease in singlet oxygen generation rate, particularly in the initial 40 seconds, was noted. Notably, MB/Ag NPs exhibited faster decrease in absorbance values compared to MB/Ag NPs/reserpine, suggesting higher initial singlet oxygen production up to 60 seconds, but both reached similar absorbance values after 90 seconds.

Overall, the results of singlet oxygen generation measurements indicate that reserpine neither enhances nor diminishes singlet oxygen production after 90 seconds, whether Ag NPs are present or not. Therefore, it can be inferred that the mechanism behind enhanced bacterial photodeactivation is likely due to efflux pump inhibition rather than any direct effect on singlet oxygen generation by reserpine.

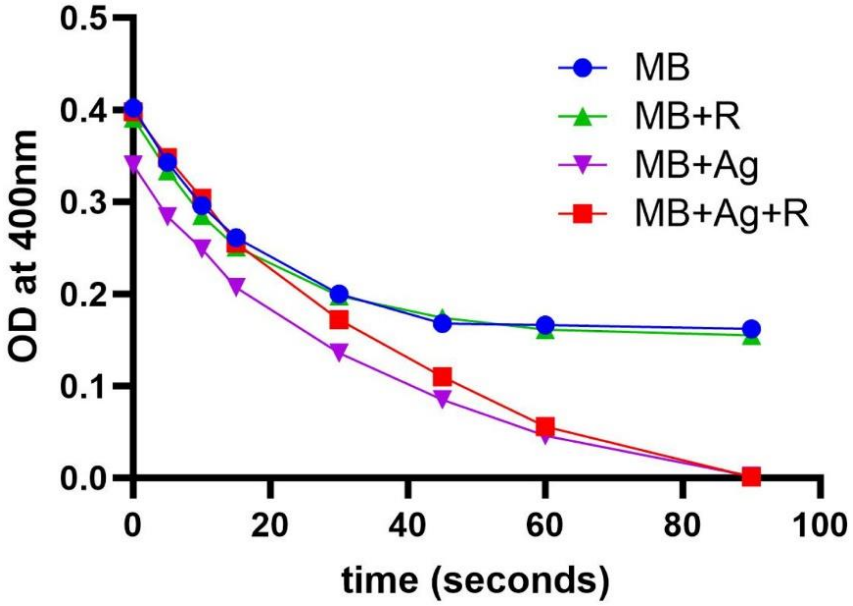

Figure 10 Optical density measurements of ABMDMA solution at various irradiation times with MB, reserpine, and/or Au NPs in solution.

3.6 Deactivation of MB over time (in cysteine)

In previous studies, we demonstrated that MB loses effectiveness in the presence of albumin and cysteine, exhibiting significantly lower deactivation rates in plasma compared to water, saline, and PBS solutions [61]. This reduced deactivation rate was attributed to cysteine's interaction with the electron-deficient central nitrogen in MB, leading to MB reduction. Consequently, MB in its reduced form has altered dipole moments that prevent effective light absorption for singlet oxygen production, rendering it ineffective as a bacterial killing agent, especially in human plasma [24].

To address this limitation and enhance MB's effectiveness as a PDT agent, MB has been conjugated to various carriers, including nanomaterials and quantum dots [25,54,62]. Here, we aimed to investigate if reserpine could mitigate the ineffectiveness of MB in the presence of cysteine, an essential component of albumin, a major human plasma protein.

Figure 11 illustrates the decrease and recovery of the 660 nm absorption band of MB in PBS and cysteine solutions. Albumin's cysteine component, with its nucleophilic thiolate anion, readily reacts with the electron-deficient central nitrogen in MB, leading to the formation of a benzoic non-ionic species with a reduced absorption cross-section at 660 nm. This process diminishes MB's ability to produce triplet and singlet oxygen.

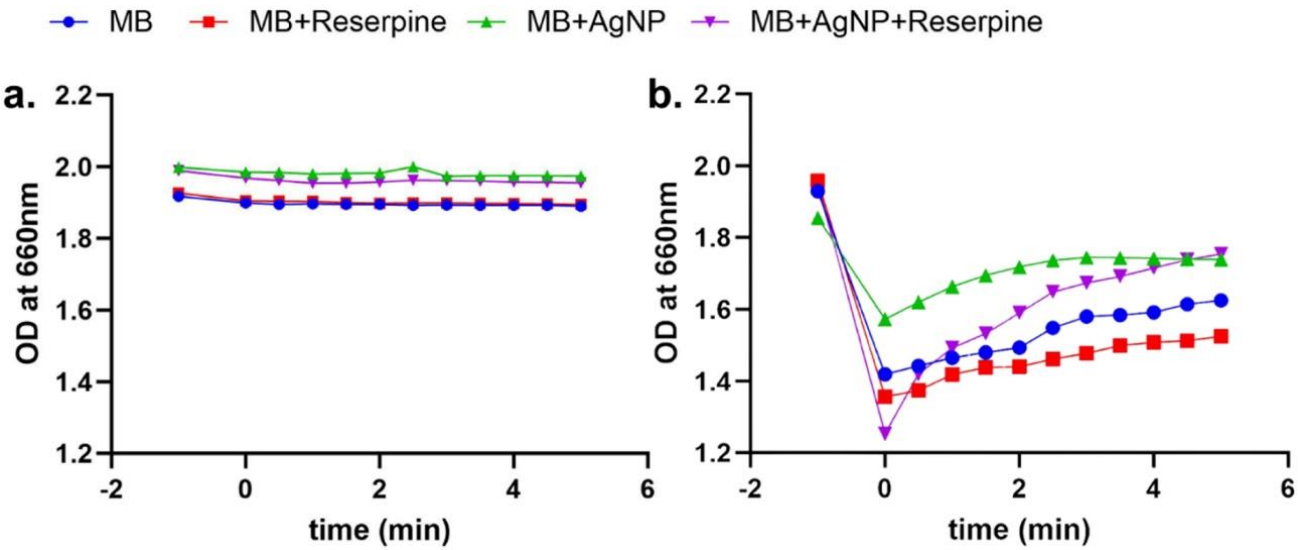

Figure 11 Optical density measurements of methylene blue at 660 nm before and after 1-minute irradiation under 660 nm red light with reserpine and/or Ag NPs in a)PBS and b) cysteine solution.

Interestingly, when reserpine was added to MB, the 660 nm band decreased further, indicating reduced singlet oxygen production. A similar trend of decreased initial absorbance was observed with MB/Ag NPs when reserpine was added, suggesting lower singlet oxygen production. These findings align with our previous observations of singlet oxygen generation,

indicating that reserpine does not enhance MB's singlet oxygen production; rather, it appears to have a negative effect on singlet oxygen production.

Therefore, the mechanism through which reserpine improves PDT efficacy is likely due to its inhibition of the AcrAB-TolC efflux pump, thereby preventing the removal of MB. It is also plausible that Ag NPs similarly inhibit the AcrB pump, as observed with copper nanoparticles[34]. This dual inhibition of efflux pumps by reserpine and possibly Ag NPs contributes to the improved effectiveness of PDT observed in our experiments.

3.7 Molecular docking of reserpine and MB into AcrB

The AcrAB-TolC efflux system is essential for drug resistance in *E. coli*, comprising the AcrB component, a homotrimeric H+\drug antiporter located on the inner membrane. AcrB works in conjunction with AcrA and TolC to actively transport various antibiotics and photosensitizers out of the cell. Studies have identified four distinct channels (CH1-CH4) through which substrates enter, contributing to the system's ability to recognize and transport a broad spectrum of substrates [63].

Planar aromatic cations like MB and ethidium bromide are thought to preferentially bind to the CH3 channel among others [64]. However, detailed investigations specifically on AcrB interactions with MB are lacking in current literature.

To address this gap, we conducted molecular docking studies to comparatively analyze the interactions of AcrB with MB and reserpine, depicted in Figure 13. The binding energies for

Ligands	Pose 1	Pose 2	Pose 3	Pose 4	Pose 5	Pose 6	Pose 7	Pose 8	Pose 9
Reserpine	−9.4	−9.4	−9.0	−8.9	−8.4	−8.4	−8.4	−8.3	−8.3
Methylene Blue	−7.2	−7.1	−7.0	−7.0	−6.9	−6.7	−6.6	−6.6	−6.5

Figure 12 Predicted binding energies (in kcal/mol) of all 9 poses for reserpine and methylene blue with E.coli AcrB.

nine poses of reserpine and MB are detailed in Figure 12, indicating that reserpine exhibits stronger interactions than MB at the CH3 active site.

Our results reveal that reserpine forms hydrogen bonds with SER48, THR87, and ARG620 of AcrB, along with a pi-pi interaction with PHE178. In contrast, MB primarily engages in pi-pi interactions with PHE178, PHE610, PHE615, and PHE628. Specifically, the binding affinity of the first pose of reserpine was determined to be -9.4 kcal/mol, consistent with previous literature[65]. Comparatively, MB demonstrated a binding affinity of -7.2 kcal/mol,

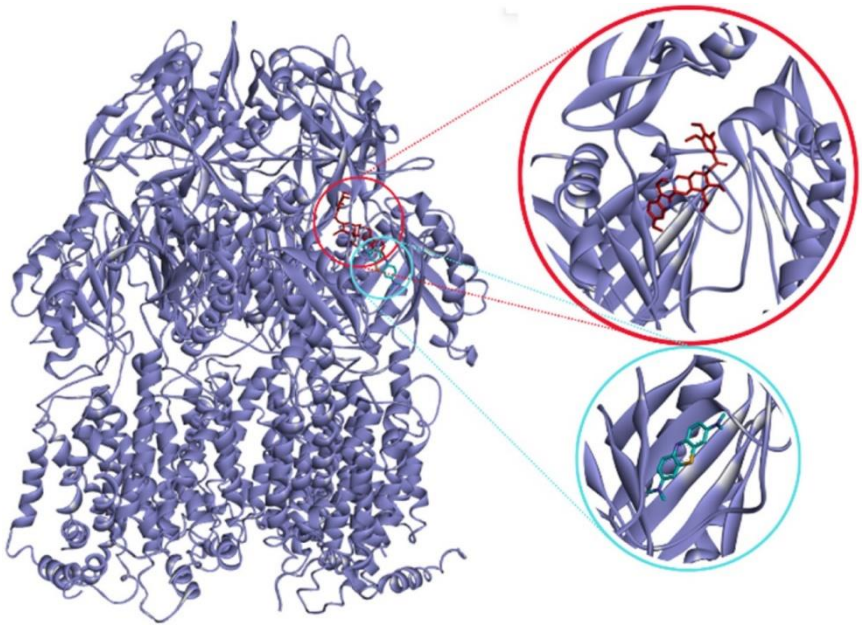

Figure 13. Graphical representation of the AcrB protein. The red and blue insets represent the active sites for reserpine and methylene blue respectively.

indicating that reserpine exhibits a higher overall affinity for the AcrB component than MB.

These findings suggest that reserpine acts as a competitive inhibitor, potentially preventing MB from binding effectively to AcrB. This molecular insight supports the hypothesis that reserpine enhances PDT efficacy by inhibiting the AcrAB-TolC efflux pump, thereby increasing the intracellular concentration of MB available for bacterial photodeactivation.

CONCLUSION

Our study investigates the synergistic effects of reserpine, EPI, in conjunction with Ag NPs and MB as agents in PDT against Gram-negative bacteria, specifically *Escherichia coli*. The findings demonstrate that the inclusion of reserpine significantly enhances the antibacterial efficacy of PDT. This improvement is attributed to the inhibition of the AcrAB-TolC efflux pump by reserpine, preventing the removal of MB from bacterial cells, thereby increasing the intracellular concentration of the photosensitizer.

Experimental results show that the combination of MB, Ag NPs, and reserpine achieves a higher rate of bacterial deactivation compared to MB and Ag NPs alone. Molecular docking studies further support this by revealing a higher binding affinity of reserpine to the AcrB component of the efflux pump compared to MB. This competitive inhibition by reserpine blocks the efflux pathway, enhancing the retention and effectiveness of MB within bacterial cells.

Interestingly, the study also indicates that the size of Ag NPs does not significantly impact the efficacy of reserpine in PDT, suggesting that the primary mechanism of action is through efflux pump inhibition rather than variations in nanoparticle size. Additionally, the research shows that reserpine does not contribute to an increase in singlet oxygen production, which is a critical factor in PDT. Instead, the enhanced antibacterial effect is primarily due to the prevention of MB efflux, ensuring higher intracellular photosensitizer concentrations.

APPENDIX A: SAMPLE PREPARATIONS AND ADDITIONAL PROCEDURES

i. Preparation of MB Stock Solution (6.1 x 10^{-4} M)

To prepare a stock solution of MB, 1.140 g of crystalline MB (MB • 3H2O, molecular weight 373.90 g/mol, Sigma Aldrich) was measured using an electronic scale with 0.1 mg sensitivity. The weighted compound was placed into a 50 mL centrifuge tube, and 50 mL of autoclaved deionized water was added. The tube was shaken until the compound fully dissolved. The centrifuge tube was then covered with aluminum foil to prevent photobleaching.

ii. Preparation of MB Experimental Solution (6.1 x 10^{-5} M)

Experimental solutions of MB were prepared by taking 5 mL of the MB stock solution (6.1 x 10^{-4} M) and placing it in a 50 mL centrifuge tube. Then, 45 mL of autoclaved deionized water were added to dilute the solution to a final concentration of 6.1 x 10^{-5} M. Similar to the stock solution, the experimental solution tube was covered with aluminum foil to prevent photobleaching.

iii. Preparation of Sodium Citrate Solution (2 mM)

A 2 mM aqueous solution of sodium citrate was prepared by weighing 588.2 mg of sodium citrate (molecular weight 294.09 g/mol, Fisher) and placing it into a 1,000 mL volumetric flask. Then, deionized water was added up to the 1,000 mL mark. The solution was stirred with a magnetic stir bar and magnetic stir plate until the sodium citrate was completely dissolved. Finally, the solution was transferred to a 1 L screw-top bottle and stored at room temperature for use in pulsed laser ablation.

iv. Preparation of Phosphate Buffer Solution (pH = 7.4)

To prepare the phosphate buffer solution, we began by weighing out 0.2108 grams of potassium phosphate monobasic (molecular weight 136.09 g/mol, purity ≥ 99.0%, sourced from Sigma Aldrich), 0.729 grams of sodium phosphate dibasic (molecular weight 141.96 g/mol, purity ≥ 99.0%, also from Sigma Aldrich), and 9.0054 grams of sodium chloride (molecular weight 58.44 g/mol, BioXtra grade, purity ≥ 99.5%, Sigma Aldrich). These components were placed into a 1,000 mL volumetric flask. Deionized water was then added up to the calibration mark. Using a magnetic stir bar and magnetic plate, the solution was stirred until all solids were fully dissolved. Afterward, the solution was transferred into a 1-liter screw-top bottle and subjected to autoclaving for approximately 60 minutes, utilizing the Liquid15 Cycle.

v. Preparation of Reserpine Solution

To prepare a 20 µM solution of Reserpine, 608.68 micrograms of Reserpine (molecular weight 608.68 g/mol, sourced from Millipore Sigma) was accurately weighed and dissolved in 500 µL of DMSO within a 50 mL centrifuge tube. Subsequently, 49.5 mL of autoclaved deionized water was added to the tube. The resulting mixture was thoroughly mixed by shaking, ensuring complete dissolution. The tube was then covered with aluminum foil to protect the solution from light and stored at room temperature for future use.

vi. Preparation of ABMDMA Solution

To prepare a 2.4 mM solution of ABMDMA, weigh 10 mg of ABMDMA (molecular weight 410.37 g/mol, from Sigma Aldrich) and place it into a 10 mL volumetric flask. Add deionized water to fill approximately half of the flask, swirling the flask to facilitate dissolution.

Once the compound is completely dissolved, add deionized water up to the mark. Transfer the solution to a capped vial, cover it with aluminum foil, and store it at 4°C.

vii. Measurement of Experimentally Produced Ag NPs Concentration

The concentration of experimentally produced Ag NPs was determined using the Beer-Lambert technique. A commercial standard solution of Ag NPs in citrate with an average diameter of 10 nm (0.05 mg/mL, purchased from NanoComposix) was used. Solutions with concentrations of 0.05, 0.04, 0.03, 0.02, 0.01, and 0.005 mg/mL were prepared by adding 1,000 µL, 800 µL, 600 µL, 400 µL, 200 µL, and 100 µL of the commercial Ag NPs solution into separate 1.5 mL microcentrifuge tubes, respectively. A 2 mM citrate solution was then added to each tube to achieve a final volume of 1 mL. Sodium citrate was used as a blank in UV-Vis spectroscopy, and the absorbance of each standardized solution was recorded at 518 nm. A plot of absorbance versus concentration was generated, yielding a linear equation of $y = mx + b$. The absorbance of the experimentally produced Ag NP solution was measured at 518 nm, and this value was used as the y-value in the linear equation to solve for x, which corresponds to the concentration of Ag NPs.

viii. Preparation of LB Agar Media

To prepare LB agar medium, add 0.250 L of deionized water to a 1 L Erlenmeyer flask. Weigh out 20 g of Luria-Bertani (LB) agar powder (Miller, Difco TM) and place it in the flask. Add another 0.250 L of deionized water to the flask and mix the solution using a magnetic stir bar and stir plate until it is completely dissolved. Once dissolved, cover the flask with aluminum foil, secure it with autoclave tape, and autoclave for approximately 60 minutes using the Liquid 15 cycle. After the autoclave cycle was finished, thermal-resistant gloves were used to carefully

remove the flasks, which were then placed in a bead bath maintained at 70°C (NOTE: The glassware will be hot). While the agar solution remained in the bead bath, single-use sterile petri dishes were arranged in a biological hood. The flask containing the agar solution was removed from the bead bath and cooled slightly by running room-temperature tap water over its exterior for about 30 seconds. The agar solution was then poured into the petri dishes, ensuring the bottom of each dish was covered. The plates were left uncovered in the biological hood for approximately 15 minutes to cool. After cooling, lids were placed on each plate. The plates were stacked upside down, placed in a plastic sleeve, and stored in the refrigerator for future use. NOTE: Storing the plates upside down prevents condensation from forming on the lids.

ix. Preparation of LB Broth Media

To prepare Luria-Bertani (LB) broth, start by placing 250 mL of deionized (DI) water into a 1,000 mL Erlenmeyer flask. Accurately weigh out 10 g of agar powder using an analytical balance, ensuring precision, and then add this to the flask containing the DI water. Subsequently, add an additional 250 mL of DI water to the flask. This additional water helps rinse any agar powder that may have adhered to the sides of the flask, ensuring all the powder is incorporated into the solution.

Place a magnetic stir bar into the flask, and set the flask on a magnetic stir plate. Stir the mixture until the agar is completely dissolved, ensuring there are no visible particles and the solution is homogeneous. This process may take several minutes, so patience and careful observation are necessary. Once the agar is fully dissolved, remove the flask from the stir plate and retrieve the magnetic stir bar using a clean utensil to avoid contamination.

Cover the top of the flask with a piece of aluminum foil, ensuring it is tightly secured to prevent any contaminants from entering. Apply autoclave tape around the foil to further secure it and to act as an indicator of successful sterilization. Autoclave the solution using a Liquid15 cycle for approximately 60 minutes. This step is crucial for sterilizing the medium, ensuring it is free from any microbial contaminants.

After the autoclaving cycle is complete and the flask has cooled sufficiently, transfer the sterilized solution into a sterilized 1-liter bottle. This transfer should be done carefully to avoid introducing any contaminants. Store the bottle at room temperature, in a clean and dry environment, until it is ready for use.

x. Inoculation of *E. coli*

To generate a liquid culture of *E. coli*, begin by measuring 5 mL of LB broth in a biological safety hood. This should be done using a new, sterile 10 mL glass pipette and an electric pipetman to ensure accuracy and sterility. Transfer the measured LB broth into a new, sterile 15 mL centrifuge tube.

Since LB broth is highly susceptible to contamination, it is essential to flame sterilize the lid and rim of the LB broth container both when opening and before closing it. This practice helps maintain the sterility of the remaining broth.

Next, sterilize a metal inoculating loop. First, clean it with a paper towel soaked in an appropriate cleaner. Then, sterilize the loop end by dipping it in ethanol and passing it through a Bunsen burner flame until the ethanol burns off. Allow the loop to cool for 15-30 seconds to prevent killing the bacteria by heat.

Once cooled, use the loop to collect a single *E. coli* colony from a stock plate. Gently touch the colony with the loop end and then directly insert the loop into the centrifuge tube containing the LB broth. Swirl the loop in the broth for 10-15 seconds to ensure the bacteria are transferred into the solution. After transferring the bacteria, flame sterilize the inoculating loop again to eliminate any residual bacteria.

Cap the centrifuge tube securely and place it in an incubator set to 37 °C and 200 rpm. Incubate the tube for 18-24 hours, allowing the bacteria to grow and multiply. After handling the culture, sterilize the biological hood and all materials used within it with Amphyl cleaner on a paper towel to maintain a sterile environment.

xi. Preparation of New *E. coli* Stock Plate

To maintain a consistent supply of *E.coli* cultures, new stock plates should be prepared every 2-4 weeks. Start by generating a liquid culture of *E. coli* following the inoculation procedure described above. After the incubation period, transfer to a biological safety hood to continue working under sterile conditions.

Sterilize an inoculating loop as previously described, ensuring it is free from contaminants. Dip the loop into the liquid culture to collect a sample. Streak the loop onto a new agar plate using the quadrant streak method or another preferred pattern to promote isolated colony formation. This technique helps in obtaining single colonies that can be used for future inoculations.

Incubate the streaked agar plate at 37 °C for 18-24 hours to allow the bacteria to grow and form visible colonies. After the incubation period, store the plate in a BSL-1 refrigerator for

future use. This storage helps preserve the bacteria and ensures they are available for future experiments.

As a final step, clean the biological hood and any materials used during the process with Amphyl cleaner on a paper towel to maintain a sterile environment and prevent contamination of future cultures.

xii. Bacteria Concentration Standardization Procedure

To standardize the bacteria concentration before initiating the photodeactivation experiment, begin by preparing a liquid culture of *E. coli* as described in the previous procedures. Once the liquid culture is ready, measure 3.0 mL of the culture using a sterile pipette and transfer it into a clean, disposable cuvette. Cover the cuvette securely with parafilm to prevent any contamination or spillage.

Next, measure the absorbance of the bacterial solution at a wavelength of 600 nm using a spectrophotometer. Ensure that fresh LB broth is used as the blank for calibration purposes. The target optical density (OD) for the bacterial solution is 1.7 OD at 600 nm. If the measured absorbance is below the target, return the culture to the incubator and allow it to incubate for a longer period. Periodically recheck the absorbance until the target OD of 1.7 is achieved, ensuring the bacterial concentration is standardized for the experiment.

xiii. Detailed Bacteria Irradiation Procedure

As detailed in section 2.5, the photodeactivation of bacteria in the presence of various compounds was examined. Begin by preparing a liquid culture of *E. coli* and standardizing its concentration as described in procedures ix and xi. Once the bacterial solution is ready, proceed to prepare the experimental solutions.

In a sterile 6-well plate, add the following volumes to each well according to the experimental conditions: 100 µL of the standardized bacteria solution, 500 µL of Ag NPs, and/or 50 µL of MB. Adjust the total volume of each well to 1,000 µL by adding phosphate-buffered saline (PBS) to make up the remaining volume after the addition of bacteria, Ag NPs, and MB.

After preparing the experimental solutions, cover the 6-well plate with aluminum foil to protect it from light exposure and place it on a shaker plate. Mix the solutions at 100 rpm for 10 minutes to ensure thorough mixing of all components. Following the mixing period, remove the aluminum foil and turn on the red light source for irradiation. Maintain the plate at a distance of 9 cm from the light source throughout the irradiation process, ensuring consistent exposure across all wells.

Irradiate the plate for 5 minutes while continuing to mix on the shaker plate to ensure uniform exposure. After irradiation, take 100 µL of each experimental solution and transfer it into separate 1.5 mL microcentrifuge tubes containing 900 µL of PBS to begin the serial dilution process. Vortex each tube briefly to mix the contents thoroughly.

Perform serial dilutions by transferring 100 µL from the first microcentrifuge tube into a second tube containing 900 µL of PBS, vortexing each time to mix. Repeat this dilution process for a total of 5 microcentrifuge tubes, ensuring to change the pipette tip between each transfer to maintain accuracy and prevent cross-contamination.

Once the serial dilutions are complete, take 50 µL from each microcentrifuge tube and carefully spread it onto a new petri dish. Sterilize the metal spreader by passing it through a flame before spreading each plate to ensure sterility. Label the petri dishes accordingly and place them upside-down in an unsealed plastic bag.

Incubate the plates at 37 °C for 18-24 hours to allow bacterial colonies to grow. After the incubation period, remove the plates and count the colonies to assess the effectiveness of the photodeactivation process.

xiv. Calculation of CFU/mL After Irradiation and Incubation

To determine the colony-forming units per milliliter (CFU/mL) after irradiation, follow these steps to count and analyze the plates obtained from the serial dilution and incubation process:

1. Counting Colonies: Begin by examining the plates to identify those with easily countable colonies. Plates where individual colonies are well-separated should be selected for counting. If the colonies are numerous but still separable, label the plate as "TNTC" (Too Numerous To Count). If individual colonies are not distinguishable and form a continuous layer, label the plate as "Lawn."

2. Performing Dilution Calculations: For plates with a countable number of colonies, calculate the CFU/mL of the original solution using the dilution factor. The volume placed on each plate was 50 µL (0.05 mL). Therefore, divide the number of colonies by 0.05 mL to get the number of colonies per milliliter. Multiply this value by the dilution factor to obtain the CFU/mL of the original solution after irradiation.

For example, if the 5th serial dilution plate contains 16 colonies, the calculation would be as follows:

$$(30\ colonies/0.05\ mL)\ (100{,}000) = 6.0 \times 10^{7}\ CFU/mL$$

xv. TEM Grid Preparation

To prepare Transmission Electron Microscopy (TEM) grids for imaging, follow this detailed procedure:

1.Cleaning the Grids: Select 10-12 copper grids (SPI, 300 mesh, 3 mm) and sequentially wash them in hydrochloric acid, deionized (DI) water, and acetone. Ensure thorough washing at each step. Place the cleaned grids on filter paper within a petri dish to dry.

2.Preparing the Microscope Slide: Soak a microscope slide (Fisherbrand, Plain precleaned) in a soap solution for 3-5 minutes. Meanwhile, prepare a plastic dispense column by washing it with a "wash solution" (ethylene dichloride) and then filling it to the mark with "Gold solution" (1% formvar in 1,2-dichloroethylene).

3. Coating the Slide: Remove the soaked slide from the solution and dry it using lens paper. Insert the slide vertically into the column filled with "Gold solution" and allow it to sit for 30-45 seconds. After this period, open the valve to recollect the "Gold solution." Remove the slide, place the bottom end on a paper towel to absorb excess solution, and hold it vertically for 1-2 minutes to allow the solution to dry onto the slide.

4. Releasing the Formvar Film: Scratch the edges of the slide 3-5 times with a razor to facilitate the release of the formvar film. Breathe on the slide and slowly, vertically dip it into a container of DI water. The thin formvar films will separate from the slide.

5. Collecting the Grids: Place the TEM grids, bright side down, onto the gold portion of the thin films. Use a piece of parafilm to collect the grids by immersing it directly next to the formvar films at an angle, allowing the film to attach to the parafilm. Place this setup on a paper towel to dry and then store the grids on filter paper within a petri dish for future use.

6. Loading the TEM Grids: When ready to use, trace around a single grid with a pair of tweezers to isolate it. Hold the grid with tweezers secured by an O-ring. Pipette 3 μL of the Ag NPs solution onto the grid and allow it to air dry completely. Once dried, load the grid into the TEM for imaging.

Following this procedure will ensure that the TEM grids are properly prepared and ready for high-quality imaging.

xvi. Detailed ROS Measurement Procedure

To determine the reactive oxygen species (ROS) produced in solution, follow this detailed procedure:

1. Preparation of Blank Solution: Begin by placing 800-1000 μL of phosphate-buffered saline (PBS) into a 1.5 mL plastic cuvette. This cuvette will serve as the blank for the UV-Vis spectrophotometer at a wavelength of 400 nm. Measure and record the absorbance of the PBS blank to ensure accurate calibration of the instrument.

2. Preparation of Experimental Solutions: In separate 1.5 mL plastic cuvettes, combine the following volumes to create the experimental solutions:

- 100 μL of ABMDMA solution
- 500 μL of Ag NPs
- 50 μL of MB
- 50 μL of Reserpine solution

Adjust the final volume of each cuvette to 1,000 µL by adding PBS. This ensures consistency across all experimental solutions. Mix each solution thoroughly by gently tapping the cuvette.

3. Initial Absorbance Measurement: Measure and record the initial absorbance of each experimental solution at 400 nm using the UV-Vis spectrophotometer. This serves as the baseline absorbance before irradiation.

4. Irradiation and Mixing: Cover each cuvette securely with parafilm to prevent contamination and evaporation. Place the cuvettes at a fixed distance of 9 cm from the light source. Ensure that the cuvettes are well-positioned on a shaker plate set to 100 rpm to facilitate uniform mixing during irradiation.

5. First Irradiation Cycle: Irradiate the cuvettes for 5 seconds. Immediately after irradiation, measure and record the absorbance of each cuvette at 400 nm.

6. Subsequent Irradiation Cycles: Return the cuvettes to the shaker plate and irradiate them for an additional 5 seconds. Measure and record the absorbance after each irradiation cycle. Continue this process, repeating the irradiation and absorbance measurement steps until the desired number of data points has been collected. Typical time intervals for data collection include: 5, 10, 15, 30, 45, 60, 90, 120, 180, 240, 300, 360, 420, 480, 540, and 600 seconds.

By meticulously following this procedure, you will be able to accurately determine the amount of ROS produced in the experimental solutions over time, providing valuable data for your analysis.

APPENDIX B: LASER OPERATIONS

i. Operation of Nanosecond Laser

Before operating the nanosecond laser, ensure the following safety protocols are strictly adhered to:

1. Safety Preparations:

- Post the “Danger: Laser in Use” sign outside the laboratory.

- Notify all personnel within the lab about the laser operation.

- Ensure all personnel put on appropriate laser safety goggles.

2. Turning on the Laser:

- Turn the key-switch 90° counterclockwise to the ON position. The Laser ON light should illuminate, indicating the laser is powered.

- Allow the laser to warm up for approximately 5 minutes.

3. Setting the Q-Switch:

- After the warm-up period, set the Q-switch value by pressing the SELECT button until the Q-SW DELAY LED indicator light turns on.

- Adjust the Q-switch value using the UP and DOWN buttons. Note that increasing the Q-switch value decreases the output power. For synthesis procedures, a Q-switch value of 200 is recommended.

4. Setting the Frequency:

- Press the SELECT button until the screen displays F10.

- Adjust the frequency using the UP and DOWN buttons if necessary. For synthesis procedures, set the frequency to 10 Hz.

5. Checking the Pulse Mode:

- Press the SELECT button until the screen reads P00 or P01.

- If set to P00, press the single shot controller button once to switch to P01.

- Press the START/STOP button to initiate the laser operation. A continuous clicking sound should indicate that the laser is active.

- Allow the laser to run for an additional 5 minutes before proceeding.

6. Opening the Shutters:

- After the additional warm-up period, open the first shutter by pressing the SHUTTER button once.

- Manually slide the second shutter on the front of the laser from the closed to the open position.

7. Adjusting the Q-Switch During Operation:

- If adjustments to the Q-switch value are necessary during laser operation:

  - Close both shutters.

  - Switch the mode from P00 to P01 by pressing the UP button.

  - Stop the laser by pressing the START/STOP button.

- Adjust the Q-switch value as previously described.

- Change the mode back to P00 and restart the laser by pressing the START/STOP button.

- Reopen the shutters to resume operation.

8. Laser Alignment:

- Use the single shot controller to emit single or continuous shots for alignment.

- Place burn paper covered with a single layer of clear tape in front of each mirror and lens to prevent dust accumulation and aid in alignment.

- Ensure the laser beam is centered on each mirror or lens to achieve the desired effect, minimize interference, and prevent uncontrolled beams.

- Test the laser power using a power meter before the converging lens. Caution: Never use the power meter after a converging lens to avoid damaging the meter.

9. Adjusting Laser Power:

- Utilize a halfwave plate and polarizer to adjust the laser power.

- The polarizer splits the beam into a straight path and a perpendicular path. Ensure the perpendicular reflection is blocked by a beam dump.

- Rotate the halfwave plate clockwise or counterclockwise to control the power of the straight beam.

10. Turning off the Laser:

- Press the START/STOP button to cease laser operation.

- Close both the first and second shutters.

- Change the mode from P00 to P01.

- Wait for 5 minutes to allow the laser to cool down.

- Turn the key switch 90° clockwise to the OFF position.

By following these detailed steps, you can ensure the safe and effective operation of the nanosecond laser for your experiments.

REFERENCES

1. https://www.cdc.gov/drugresistance/biggest-threats.html.

2. Antibiotic Resistance Threats in the United States. *Cent Dis Control Prev US U S Dep Health Hum Serv*. Published online 2013. https://www.hsdl.org/c/antibiotic-resistance-threats-in-the-united-states/

3. Reardon S. Antibiotic alternatives rev up bacterial arms race. *Nature*. 2015;521(7553):402-403. doi:10.1038/521402a

4. Lucky SS, Soo KC, Zhang Y. Nanoparticles in Photodynamic Therapy. *Chem Rev*. 2015;115(4):1990-2042. doi:10.1021/cr5004198

5. Hamblin MR, Hasan T. Photodynamic therapy: a new antimicrobial approach to infectious disease? *Photochem Photobiol Sci*. 2004;3(5):436-450. doi:10.1039/b311900a

6. Gilaberte Y, Rezusta A, Juarranz A, Hamblin MR. Editorial: Antimicrobial Photodynamic Therapy: A New Paradigm in the Fight Against Infections. *Front Med*. 2021;8:788888. doi:10.3389/fmed.2021.788888

7. Hamblin MR, Huang YY, eds. *Handbook of Photomedicine*. CRC Press; 2014.

8. Bulina ME, Chudakov DM, Britanova OV, et al. A genetically encoded photosensitizer. *Nat Biotechnol*. 2006;24(1):95-99. doi:10.1038/nbt1175

9. Boyle RW, Dolphin D. Structure and Biodistribution Relationships of Photodynamic Sensitizers*. *Photochem Photobiol*. 1996;64(3):469-485. doi:10.1111/j.1751-1097.1996.tb03093.x

10. Zeina B, Greenman J, Purcell WM, Das B. Killing of cutaneous microbial species by photodynamic therapy. *Br J Dermatol*. 2001;144(2):274-278. doi:10.1046/j.1365-2133.2001.04013.x

11. Wainwright M. Photodynamic antimicrobial chemotherapy (PACT). *J Antimicrob Chemother*. 1998;42(1):13-28. doi:10.1093/jac/42.1.13

12. Dai T, Huang YY, Hamblin MR. Photodynamic therapy for localized infections—State of the art. *Photodiagnosis Photodyn Ther*. 2009;6(3-4):170-188. doi:10.1016/j.pdpdt.2009.10.008

13. Müller-Breitkreutz K, Mohr H, Briviba K, Sies H. Inactivation of viruses by chemically and photochemically generated singlet molecular oxygen. *J Photochem Photobiol B*. 1995;30(1):63-70. doi:10.1016/1011-1344(95)07150-Z

14. Ganash EA. Synthesis of silver nanoparticles using pulsed laser ablation in liquid: a review. *Laser Phys Lett*. 2023;20(1):013001. doi:10.1088/1612-202X/acab57

15. Semaltianos NG. Nanoparticles by Laser Ablation. *Crit Rev Solid State Mater Sci*. 2010;35(2):105-124. doi:10.1080/10408431003788233

16. Rafique M, Rafique MS, Kalsoom U, Afzal A, Butt SH, Usman A. Laser ablation synthesis of silver nanoparticles in water and dependence on laser nature. *Opt Quantum Electron*. 2019;51(6):179. doi:10.1007/s11082-019-1902-0

17. Mafuné, F, Kohno J ya, Takeda Y, Kondow T, Sawabe H. Formation and Size Control of Silver Nanoparticles by Laser Ablation in Aqueous Solution. *J Phys Chem B*. 2000;104(39):9111-9117. doi:10.1021/jp001336y

18. Ganash EA, Altuwirqi RM. Size Control of Synthesized Silver Nanoparticles by Simultaneous Chemical Reduction and Laser Fragmentation in Origanum majorana Extract: Antibacterial Application. *Materials*. 2021;14(9):2326. doi:10.3390/ma14092326

19. Samir A, Abd El-salam HM, Harun SW, Mohamed T. The effects of different parameters and interaction angles of a 532 nm pulsed Nd: YAG laser on the properties of laser-ablated silver nanoparticles. *Opt Commun*. 2021;501:127366. doi:10.1016/j.optcom.2021.127366

20. Unser S, Bruzas I, He J, Sagle L. Localized Surface Plasmon Resonance Biosensing: Current Challenges and Approaches. *Sensors*. 2015;15(7):15684-15716. doi:10.3390/s150715684

21. Nikov RG, Dikovska AO, Nedyalkov NN, Avdeev GV, Atanasov PA. Au nanostructure fabrication by pulsed laser deposition in open air: Influence of the deposition geometry. *Beilstein J Nanotechnol*. 2017;8:2438-2445. doi:10.3762/bjnano.8.242

22. Dorranian D, Tajmir S, Khazanehfar F. Effect of Laser Fluence on the Characteristics of Ag Nanoparticles Produced by Laser Ablation. *Soft Nanosci Lett*. 2013;03(04):93-100. doi:10.4236/snl.2013.34017

23. Valverde-Alva MA, García-Fernández T, Villagrán-Muniz M, et al. Synthesis of silver nanoparticles by laser ablation in ethanol: A pulsed photoacoustic study. *Appl Surf Sci*. 2015;355:341-349. doi:10.1016/j.apsusc.2015.07.133

24. Hakimov S, Kylychbekov S, Harness B, et al. Evaluation of silver nanoparticles attached to methylene blue as an antimicrobial agent and its cytotoxicity. *Photodiagnosis Photodyn Ther*. 2022;39:102904. doi:10.1016/j.pdpdt.2022.102904

25. Kholikov K. Enhanced Singlet Oxygen Generation and Antimicrobial Activity of Methylene Blue Coupled with Graphene Quantum Dots as an Effective Photodynamic Therapy Agent. Published online 2018.

26. Soto SM. Role of efflux pumps in the antibiotic resistance of bacteria embedded in a biofilm. *Virulence*. 2013;4(3):223-229. doi:10.4161/viru.23724

27. Zhu GH, Sun XP, Li J, et al. No association between low-dose reserpine use and depression in older hypertensive patient: result of a multicenter, cross-sectional study. *J Geriatr Cardiol JGC*. 2019;16(8):608-613. doi:10.11909/j.issn.1671-5411.2019.08.001

28. Chetri S, Bhowmik D, Paul D, et al. AcrAB-TolC efflux pump system plays a role in carbapenem non-susceptibility in Escherichia coli. *BMC Microbiol*. 2019;19(1):210. doi:10.1186/s12866-019-1589-1

29. Blanco P, Hernando-Amado S, Reales-Calderon J, et al. Bacterial Multidrug Efflux Pumps: Much More Than Antibiotic Resistance Determinants. *Microorganisms*. 2016;4(1):14. doi:10.3390/microorganisms4010014

30. Pos KM. Drug transport mechanism of the AcrB efflux pump. *Biochim Biophys Acta BBA - Proteins Proteomics*. 2009;1794(5):782-793. doi:10.1016/j.bbapap.2008.12.015

31. Alvarez-Ortega C, Olivares J, Martínez JL. RND multidrug efflux pumps: what are they good for? *Front Microbiol*. 2013;4. doi:10.3389/fmicb.2013.00007

32. Webber MA. The importance of efflux pumps in bacterial antibiotic resistance. *J Antimicrob Chemother*. 2003;51(1):9-11. doi:10.1093/jac/dkg050

33. Gaurav A, Bakht P, Saini M, Pandey S, Pathania R. Role of bacterial efflux pumps in antibiotic resistance, virulence, and strategies to discover novel efflux pump inhibitors. *Microbiology*. 2023;169(5). doi:10.1099/mic.0.001333

34. Christena LR, Mangalagowri V, Pradheeba P, et al. Copper nanoparticles as an efflux pump inhibitor to tackle drug resistant bacteria. *RSC Adv*. 2015;5(17):12899-12909. doi:10.1039/C4RA15382K

35. Khan S, Khan SN, Akhtar F, Misba L, Meena R, Khan AU. Inhibition of multi-drug resistant Klebsiella pneumoniae: Nanoparticles induced photoinactivation in presence of efflux pump inhibitor. *Eur J Pharm Biopharm*. 2020;157:165-174. doi:10.1016/j.ejpb.2020.10.007

36. Gupta D, Singh A, Khan AU. Nanoparticles as Efflux Pump and Biofilm Inhibitor to Rejuvenate Bactericidal Effect of Conventional Antibiotics. *Nanoscale Res Lett*. 2017;12(1):454. doi:10.1186/s11671-017-2222-6

37. Kulshrestha S, Khan S, Hasan S, Khan ME, Misba L, Khan AU. Calcium fluoride nanoparticles induced suppression of Streptococcus mutans biofilm: an in vitro and in vivo approach. *Appl Microbiol Biotechnol*. 2016;100(4):1901-1914. doi:10.1007/s00253-015-7154-4

38. Tegos GP, Hamblin MR. Phenothiazinium Antimicrobial Photosensitizers Are Substrates of Bacterial Multidrug Resistance Pumps. *Antimicrob Agents Chemother*. 2006;50(1):196-203. doi:10.1128/AAC.50.1.196-203.2006

39. Tegos GP, Masago K, Aziz F, Higginbotham A, Stermitz FR, Hamblin MR. Inhibitors of Bacterial Multidrug Efflux Pumps Potentiate Antimicrobial Photoinactivation. *Antimicrob Agents Chemother*. 2008;52(9):3202-3209. doi:10.1128/AAC.00006-08

40. Shirdel Z, Fekrirad Z. Efflux Pump Inhibitor Potentiates the Antimicrobial Photodynamic Inactivation of Multidrug-Resistant *Acinetobacter baumannii*. *Photobiomodulation Photomed Laser Surg*. 2024;42(4):314-320. doi:10.1089/photob.2023.0194

41. Rineh A, Bremner JB, Hamblin MR, Ball AR, Tegos GP, Kelso MJ. Attaching NorA efflux pump inhibitors to methylene blue enhances antimicrobial photodynamic inactivation of Escherichia coli and Acinetobacter baumannii in vitro and in vivo. *Bioorg Med Chem Lett*. 2018;28(16):2736-2740. doi:10.1016/j.bmcl.2018.02.041

42. Alenazy R. Drug Efflux Pump Inhibitors: A Promising Approach to Counter Multidrug Resistance in Gram-Negative Pathogens by Targeting AcrB Protein from AcrAB-TolC Multidrug Efflux Pump from Escherichia coli. *Biology*. 2022;11(9):1328. doi:10.3390/biology11091328

43. Allamyradov Y, Yosef JB, Kylychbekov S, et al. The role of efflux pump inhibitor in enhancing antimicrobial efficiency of Ag NPs and MB as an effective photodynamic therapy agent. *Photodiagnosis Photodyn Ther*. 2024;47:104212. doi:10.1016/j.pdpdt.2024.104212

44. Trott O, Olson AJ. AutoDock Vina: Improving the speed and accuracy of docking with a new scoring function, efficient optimization, and multithreading. *J Comput Chem*. 2010;31(2):455-461. doi:10.1002/jcc.21334

45. Takatsuka Y, Chen C, Nikaido H. Mechanism of recognition of compounds of diverse structures by the multidrug efflux pump AcrB of *Escherichia coli*. *Proc Natl Acad Sci*. 2010;107(15):6559-6565. doi:10.1073/pnas.1001460107

46. Durán N, Durán M, de Jesus MB, Seabra AB, Fávaro WJ, Nakazato G. Silver nanoparticles: A new view on mechanistic aspects on antimicrobial activity. *Nanomedicine Nanotechnol Biol Med*. 2016;12(3):789-799. doi:10.1016/j.nano.2015.11.016

47. Le Ouay B, Stellacci F. Antibacterial activity of silver nanoparticles: A surface science insight. *Nano Today*. 2015;10(3):339-354. doi:10.1016/j.nantod.2015.04.002

48. Radzig MA, Nadtochenko VA, Koksharova OA, Kiwi J, Lipasova VA, Khmel IA. Antibacterial effects of silver nanoparticles on gram-negative bacteria: Influence on the growth and biofilms formation, mechanisms of action. *Colloids Surf B Biointerfaces*. 2013;102:300-306. doi:10.1016/j.colsurfb.2012.07.039

49. Hwan, Soo & Lee, Hyeong-Seon & Ryu, Deok-Seon & Choi, Soo-Jae & Lee, Dong-Seok. (2010). Antibacterial Activity of Silver-Nanoparticles Against Staphylococcus Aureus and Escherichia Coli. 39.

50. Padwal P, Bandyopadhyaya R, Mehra S. Polyacrylic Acid-Coated Iron Oxide Nanoparticles for Targeting Drug Resistance in Mycobacteria. *Langmuir*. 2014;30(50):15266-15276. doi:10.1021/la503808d

51. Choi O, Deng KK, Kim NJ, Ross L, Surampalli RY, Hu Z. The inhibitory effects of silver nanoparticles, silver ions, and silver chloride colloids on microbial growth. *Water Res*. 2008;42(12):3066-3074. doi:10.1016/j.watres.2008.02.021

52. Dibrov P, Dzioba J, Gosink KK, Häse CC. Chemiosmotic Mechanism of Antimicrobial Activity of Ag^{+} in *Vibrio cholerae*. *Antimicrob Agents Chemother*. 2002;46(8):2668-2670. doi:10.1128/AAC.46.8.2668-2670.2002

53. Banoee M, Seif S, Nazari ZE, et al. ZnO nanoparticles enhanced antibacterial activity of ciprofloxacin against *Staphylococcus aureus* and *Escherichia coli*. *J Biomed Mater Res B Appl Biomater*. 2010;93B(2):557-561. doi:10.1002/jbm.b.31615

54. Chatterjee AK, Chakraborty R, Basu T. Mechanism of antibacterial activity of copper nanoparticles. *Nanotechnology*. 2014;25(13):135101. doi:10.1088/0957-4484/25/13/135101

55. Padwal P, Bandyopadhyaya R, Mehra S. Biocompatible citric acid-coated iron oxide nanoparticles to enhance the activity of first-line anti- TB drugs in *Mycobacterium smegmatis*. *J Chem Technol Biotechnol*. 2015;90(10):1773-1781. doi:10.1002/jctb.4766

56. Nallathamby PD, Lee KJ, Desai T, Xu XHN. Study of the Multidrug Membrane Transporter of Single Living *Pseudomonas aeruginosa* Cells Using Size-Dependent Plasmonic Nanoparticle Optical Probes. *Biochemistry*. 2010;49(28):5942-5953. doi:10.1021/bi100268k

57. Belekov E, Kholikov K, Cooper L, Banga S, Er AO. Improved antimicrobial properties of methylene blue attached to silver nanoparticles. *Photodiagnosis Photodyn Ther*. 2020;32:102012. doi:10.1016/j.pdpdt.2020.102012

58. Xiong Y, Liu X, Xiong H. Aggregation modeling of the influence of pH on the aggregation of variably charged nanoparticles. *Sci Rep*. 2021;11(1):17386. doi:10.1038/s41598-021-96798-3

59. Tang C, Hu P, Ma E, Huang M, Zheng Q. Heavy atom enhanced generation of singlet oxygen in novel indenofluorene-based two-photon absorbing chromophores for photodynamic therapy. *Dyes Pigments*. 2015;117:7-15. doi:10.1016/j.dyepig.2015.01.019

60. Shen X, He F, Wu J, Xu GQ, Yao SQ, Xu QH. Enhanced Two-Photon Singlet Oxygen Generation by Photosensitizer-Doped Conjugated Polymer Nanoparticles. *Langmuir*. 2011;27(5):1739-1744. doi:10.1021/la104722q

61. Oguz Er A, Chen J, Cesario TC, Rentzepis PM. Inactivation of bacteria in plasma. *Photochem Photobiol Sci*. 2012;11(11):1700-1704. doi:10.1039/c2pp25135c

62. Li R, Chen J, Cesario TC, Wang X, Yuan JS, Rentzepis PM. Synergistic reaction of silver nitrate, silver nanoparticles, and methylene blue against bacteria. *Proc Natl Acad Sci*. 2016;113(48):13612-13617. doi:10.1073/pnas.1611193113

63. Tam HK, Foong WE, Oswald C, Herrmann A, Zeng H, Pos KM. Allosteric drug transport mechanism of multidrug transporter AcrB. *Nat Commun*. 2021;12(1):3889. doi:10.1038/s41467-021-24151-3

64. Zwama M, Yamasaki S, Nakashima R, Sakurai K, Nishino K, Yamaguchi A. Multiple entry pathways within the efflux transporter AcrB contribute to multidrug recognition. *Nat Commun*. 2018;9(1):124. doi:10.1038/s41467-017-02493-1

65. Shaheen A, Afridi WA, Mahboob S, et al. Reserpine Is the New Addition into the Repertoire of AcrB Efflux Pump Inhibitors. *Mol Biol*. 2019;53(4):596-605. doi:10.1134/S0026893319040113

Copyright Permission

Name: Allamyradov, Yaran

Email (to receive future readership statistics): yaran.allamyradov485@topper.wku.edu

Type of document: ['Thesis']

Title: THE ROLE OF EFFLUX PUMP INHIBITOR IN ENHANCING ANTIMICROBIAL EFFICIENCY OF SILVER NANOPARTICLES AND METHYLENE BLUE AS AN EFFECTIVE PHOTODYNAMIC THERAPY AGENT

Keywords (3-5 keywords not included in the title that uniquely describe content): antimicrobial resistance, antimicrobial PDT, reserpine

Committee Chair: Dr. Ali Oguz Er

Additional Committee Members: Dr. Ivan Novikov Dr. Simran Banga

Select 3-5 TopSCHOLAR® disciplines for indexing your research topic in TopSCHOLAR®: Biophysics Other microbiology Biological and Chemical Physics Optics